

# Advanced 3D Monte Carlo Algorithms for Biophotonic and Medical Applications

Lewis McMillan



University of  
St Andrews

This thesis is submitted in partial fulfilment for the degree of  
PhD  
at the  
University of St Andrews

March 2019



# Declaration

I, Lewis McMillan, hereby certify that this thesis, which is approximately \*\*\*\*\* words in length, has been written by me, that it is the record of work carried out by me, or principally by myself in collaboration with others as acknowledged, and that it has not been submitted in any previous application for a higher degree.

I was admitted as a research student in September 2015 and as a candidate for the degree of PhD in September 2015; the higher study for which this is a record was carried out in the University of St Andrews between 2015 and 2019.

Date ..... Signature of candidate .....

I hereby certify that the candidate has fulfilled the conditions of the Resolution and Regulations appropriate for the degree of PhD in the University of St Andrews and that the candidate is qualified to submit this thesis in application for that degree.

Date ..... Signature of supervisor .....

Date ..... Signature of supervisor .....



# Abstract

Lorem ipsum dolor sit amet, consectetur adipiscing elit. Ut purus elit, vestibulum ut, placerat ac, adipiscing vitae, felis. Curabitur dictum gravida mauris. Nam arcu libero, nonummy eget, consectetur id, vulputate a, magna. Donec vehicula augue eu neque. Pellentesque habitant morbi tristique senectus et netus et malesuada fames ac turpis egestas. Mauris ut leo. Cras viverra metus rhoncus sem. Nulla et lectus vestibulum urna fringilla ultrices. Phasellus eu tellus sit amet tortor gravida placerat. Integer sapien est, iaculis in, pretium quis, viverra ac, nunc. Praesent eget sem vel leo ultrices bibendum. Aenean faucibus. Morbi dolor nulla, malesuada eu, pulvinar at, mollis ac, nulla. Curabitur auctor semper nulla. Donec varius orci eget risus. Duis nibh mi, congue eu, accumsan eleifend, sagittis quis, diam. Duis eget orci sit amet orci dignissim rutrum.

Nam dui ligula, fringilla a, euismod sodales, sollicitudin vel, wisi. Morbi auctor lorem non justo. Nam lacus libero, pretium at, lobortis vitae, ultricies et, tellus. Donec aliquet, tortor sed accumsan bibendum, erat ligula aliquet magna, vitae ornare odio metus a mi. Morbi ac orci et nisl hendrerit mollis. Suspendisse ut massa. Cras nec ante. Pellentesque a nulla. Cum sociis natoque penatibus et magnis dis parturient montes, nascetur ridiculus mus. Aliquam tincidunt urna. Nulla ullamcorper vestibulum turpis. Pellentesque cursus luctus mauris.



# Acknowledgements

Lorem ipsum dolor sit amet, consectetur adipiscing elit. Ut purus elit, vestibulum ut, placerat ac, adipiscing vitae, felis. Curabitur dictum gravida mauris. Nam arcu libero, nonummy eget, consectetur id, vulputate a, magna. Donec vehicula augue eu neque. Pellentesque habitant morbi tristique senectus et netus et malesuada fames ac turpis egestas. Mauris ut leo. Cras viverra metus rhoncus sem. Nulla et lectus vestibulum urna fringilla ultrices. Phasellus eu tellus sit amet tortor gravida placerat. Integer sapien est, iaculis in, pretium quis, viverra ac, nunc. Praesent eget sem vel leo ultrices bibendum. Aenean faucibus. Morbi dolor nulla, malesuada eu, pulvinar at, mollis ac, nulla. Curabitur auctor semper nulla. Donec varius orci eget risus. Duis nibh mi, congue eu, accumsan eleifend, sagittis quis, diam. Duis eget orci sit amet orci dignissim rutrum.

Nam dui ligula, fringilla a, euismod sodales, sollicitudin vel, wisi. Morbi auctor lorem non justo. Nam lacus libero, pretium at, lobortis vitae, ultricies et, tellus. Donec aliquet, tortor sed accumsan bibendum, erat ligula aliquet magna, vitae ornare odio metus a mi. Morbi ac orci et nisl hendrerit mollis. Suspendisse ut massa. Cras nec ante. Pellentesque a nulla. Cum sociis natoque penatibus et magnis dis parturient montes, nascetur ridiculus mus. Aliquam tincidunt urna. Nulla ullamcorper vestibulum turpis. Pellentesque cursus luctus mauris.

# Contents

<b>Declaration</b>	<b>iii</b>
<b>Abstract</b>	<b>v</b>
<b>Acknowledgements</b>	<b>vii</b>
<b>List of Figures</b>	<b>x</b>
<b>1 3D Phase Tracking Monte Carlo Algorithm</b>	<b>1</b>
1.1 Introduction . . . . .	1
1.2 Theory . . . . .	1
1.2.1 Huygens-Fresnel Principle . . . . .	3
1.2.2 Validation of Phase Tracking Algorithm . . . . .	4
1.3 Gaussian Beams . . . . .	7
1.4 Bessel Beams . . . . .	10
1.4.1 Validation . . . . .	12
1.5 Higher order Bessel beams . . . . .	17
1.6 Comparison . . . . .	19
1.7 Discussion . . . . .	19
1.8 Conclusion . . . . .	19



# List of Figures

- 1.1 Example of phase calculation when a photon has travelled a distance  $l$ . Figure also show an example of interference between two photons via addition of the complex amplitudes at the point  $P_0$ .
- 1.2 Illustration of the Huygens-Fresnel principle. At  $t_0$  a wave is incident on an aperture. Times  $t_1$ ,  $t_2$ , and  $t_3$  show the evolution of the wavefront using the Huygens-Fresnel principle.
- 1.3 Comparison of theory and simulation for the double slit experiment.  $\lambda$  is  $xnm$ ,  $b$  is, and  $d$
- 1.4 Fresnel diffraction at a square aperture.
- 1.5 Comparison of theory and simulation for diffraction through a square aperture in the Fresnel and Fraunhofer regimes.
- 1.6 Illustration of a Gaussian beam focusing to its waist then diverging away. Image shows the various defined properties of a Gaussian beam along side the radius of curvature changing direction at the waist.
- 1.7 Simulation setup of focusing a Gaussian beam through a lens. Lens is convex-plano and is modelled on ThorLabs LA4249 UV fused silica lens [16].
- 1.8 Results of *in-silico* experiment of focusing a Gaussian beam though a convex-plano lens.  $L_t$  is the lens thickness,  $D$  is the  $\frac{1}{e^2}$  input beam diameter,  $W_d$  is the working distance or back focal length,  $2z_{max}$  is the depth of the medium, and  $w_0$  is the beam waist.
- 1.9 Slice through the real part of the complex electric field of the *in-silico* experiment as in Fig. 1.7. Figure shows the radius of curvature changing direction at the waist as predicted by theory.
- 1.10 Illustration of  $\varphi MC$ 's ability to model spherical aberrations. Image generated using same setup as in Fig. 1.7, but with a  $D = 2\text{ mm}$ .
- 1.11 Geometry of a Bessel beam, generated by an axicon lens.  $\beta$  is the angle with the optical axis, and the angle of the conical waves.  $\alpha$  is the axicon angle.
- 1.12 Comparison of theoretical and MCRT simulation of a Bessel beams, with intensity normalised. The results from  $\varphi MC$  show good agreement with the theory.
- 1.13 Bessel beam in the far field.
- 1.14 Experimental setup for propagating a Bessel beam through a cuvette filled with varying concentrations of Intralipid 20%. Bessel beam is imaged by an  $20\times$  objective lens and a Grasshopper 3 camera.
- 1.15 Scattering properties of 20% Intralipid [21].
- 1.16 Comparison of experimental and simulation data for propagation of a Bessel beam produced by an axicon, through mediums of various turbidity. Images a) to g) is the data from  $\varphi MC$ , and h) to n) are the experimental data. Volumes along the top is the volume of Intralipid in each solution as in Table 1.1. All images cropped so they are the same size.

- 1.17 Comparison of a larger medium,  $2\text{ mm}^3$  versus that of a smaller medium,  $0.5\text{ mm} \times 0.5\text{ mm} \times 0.00\text{ mm}$ .
- 1.18 Helical delay element attached to an axicon. Axicon introduces an additional radial delay in addition to that of the helical element. Input beam is a Gaussian, output beam is a higher order Bessel beam,  $l > 0$ .
- 1.19 Higher order Bessel beams. a) to d) show the phase shift due to the helical element. e) to h) show line plots of the simulation data compared to the theory. i) to l) and m) to p) show the higher order Bessel beam images for theory and simulation data respectively.

# Chapter 1

## 3D Phase Tracking Monte Carlo Algorithm

### 1.1 Introduction

Complex shaped light beams have been used for a variety of tasks in biophotonics. From using Airy beams to move particles and cells [1], Bessel beam ‘tractor beams’ [2], using Airy and Bessel beams for better field of view in light-sheet microscopy [3], and using Laguerre-Gaussian beams to optical trap optically reflective particles [4].

However simulation techniques for modelling complex shaped beams in biological tissue is lacking. Currently there are a number of techniques that can model these beams in biological tissue, however they all have downsides. These methods include diffusion approximation to the radiative transfer equation (RTE), finite difference time domain (FDTD), pseudo-spectral time-domain (PSTD), beam propagation method (BPM), and Monte Carlo radiation transfer (MCRT).

Bessel beams have been the subject of intense research since their discovery in 1987 [5, 6]. Durnin noticed that the blah blah.

This chapter examines how Bessel beams compare to other beam in a scattering medium. We investigate if the Bessel beams self-healing property has any effect in a turbid medium. We examine Bessel beams and the other beams by creating a novel MCRT algorithm that allows the tracking of a photon as it propagates through a medium. The main focus of this chapter, is validation of our new novel technique, followed by using the new algorithm ( $\varphi MC$ ) to compare Gaussian and Bessel beams, to see which one performs better in a turbid medium. This chapter also extends out novel algorithm to other complex, diffraction less beams

### 1.2 Theory

The MCRT algorithm as described in ??, must be adjusted so that wave phenomena such as interference and diffraction can be modelled. Modelling these wave behaviours allows us to model complex beams, where these phenomena are required to form the beam, e.g Bessel beams. As MCRT is a ballistic simulation of photon packets, meaning that the MCRT simulation presented thus far in this thesis only modelled the ballistic behaviour of photons. However for the work presented in this chapter, wave like behaviour is crucial to modelling the various experiments and phenomena.

To convert a ballistic simulation of photon packets into a ballistic/wave-like simulation, the complex phase of each photon packet is tracked. This is achieved, by simply tracking the complex phase of the photon as it propagates through a medium. Equation (1.1) shows how the phase is calculated.

$$\varphi = \cos\left(\frac{2\pi l}{\lambda}\right) + i \sin\left(\frac{2\pi l}{\lambda}\right) \quad (1.1)$$

Where  $\varphi [-]$  is the phase of a photon packet,  $l [m]$  is the distance the photons has travelled,  $\lambda [m]$  is the wavelength of the photon, and  $i$  is the solution to  $x^2 = -1$ . Now we can calculate the phase of a photon at a position  $P_o$ , if we know the distance it has travelled, and its original phase, Fig. 1.1.

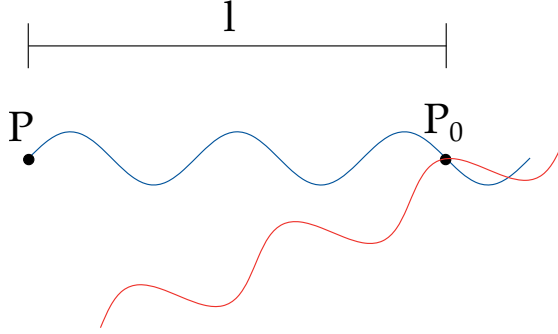


**Figure 1.1:** Example of phase calculation when a photon has travelled a distance  $l$ . Figure also show an example of interference between two photons via addition of the complex amplitudes at the point  $P_0$ .

To be able model the wave-like behaviour of photons, we let the photons packets interfere with one another in a volume or area element. We do not model the interference at a point in space where photons packets cross one another as due to the ballistic nature of the MCRT simulation, this does not occur with enough frequency in order to give a good signal to noise ratio. Thus, interference takes place in a volume,  $dV$ , or area element,  $dA$ , instead. To calculate the interference from the phase, the phase is summed in each volume or area element and the absolute value taken, and then squared. Equation (1.2) shows the equation for interference for a volume element  $dV$ . A similar relation for calculating the interference on an area element  $dA$  also exists.

$$I(\xi) = \left| \sum_{\xi} \cos\left(\frac{2\pi l}{\lambda}\right) + i \sum_{\xi} \sin\left(\frac{2\pi l}{\lambda}\right) \right|^2, \quad \xi = (x, y, z) \quad (1.2)$$

Where:

- $l$  is the total distance travelled by a photon  $[m]$ ;
- $\lambda$  is the wavelength of the photon  $[m]$ ;
- $I$  is the intensity at the  $\xi^{th}$  cell  $[Wm^{-2}]$ ;
- and  $\xi$  is the  $x^{th}$ ,  $y^{th}$ ,  $z^{th}$  cell, volume  $dV$ .

As the MCRT simulation is now a quasi ballistic/wave simulation of photon behaviour, comparisons between the simulations and, theoretical and experimental data to prove this model is accurate. However before validation of the model takes place, one further principle needs to be introduced that is required for our model to work.

### 1.2.1 Huygens-Fresnel Principle

The Huygens-Fresnel principle is a method that is used to help model the propagation of waves in the far field limit and the near field limit.

The Huygens principle states [7–9]:

“Every point on a propagating wavefront serves as the source of spherical secondary wavelets, such as the source at some time later is the envelope of these wavelets.”

The principle is illustrated in Fig. 1.2. Christiaan Huygens postulated this principle in 1678. The principle allowed Huygens to derive laws of refraction and reflection, but it failed to describe diffraction effects. This led to Augustin-Jean Fresnel in 1818, combining the Huygens principle with his own theory of interference [9, 10]. This principle, the Huygens-Fresnel principle, gave an accurate description of the propagation of light and diffraction effects. This was achieved by allowing the secondary wavelets to self interfere with one another, giving rise to an accurate description of the physical phenomena. Later, Gustav Kirchhoff gave a rigorous mathematical description of the Huygens-Fresnel principle, which is the basis of diffraction theory [11, 12].

The Huygens-Fresnel principle allows the modelling of diffraction in both the near and far field. As the principle states that every point on the wavefront is a source of secondary spherical waves, this implies that there are “backward” waves. These “backward” waves are unphysical, and there is no evidence of their existence. Thus Fresnel introduced an inclination factor to eliminate these “backward” waves. This inclination factor was later put on rigorous mathematical standing by Kirchhoff, as it naturally fell out of his theory [11, 12]. Equation (1.3) shows the equation for the complex field at a point on a plane as derived by Kirchhoff.

$$u(\mathbf{r}_1) = \frac{1}{i\lambda} \iint u(\mathbf{r}_0) \frac{\hat{\mathbf{s}}_0 \cdot (\mathbf{r}_1 - \mathbf{r}_0)}{|\mathbf{r}_1 - \mathbf{r}_0|^2} e^{ik|\mathbf{r}_1 - \mathbf{r}_0|} dS_0 \quad (1.3)$$

Where:

- $u$  is the complex electric field [ $Vm^{-1}$ ];
- $\lambda$  is the wavelength [ $m$ ];
- $S_0$  is a plane with surface normal  $\hat{\mathbf{s}}_0$  [-];
- $k$  is the wavenumber [ $m^{-1}$ ];
- and  $r_n$  are spatial coordinates [-].

Our algorithm uses the Huygens-Fresnel principle to simulate diffraction effects, that would otherwise be absent from the simulation. The principle allows the algorithm to calculate the complex amplitude at a point, and thus the intensity at that point. The Huygens-Fresnel principle is implemented by sampling the light source on the surface of any lens or in a slit. In practise this means when for example, a plane wave is incident on a slit width  $a$ , and length  $b$ , the slit area is uniformly sampled for the initial position of the photon packets. The packets are then given a random direction, sampled towards the detector thus avoiding the non-existent “backward” waves. For the case of modelling propagation through a lens, the usual geometric optics approach is taken to propagate the packets through the lens. When the packet lies on the surface of the lens, the Huygens-Fresnel principle is invoked, and the packet is given a random direction (in the direction of the medium) and propagated as usual. Essentially the Huygens-Fresnel method calculates the complex amplitude of the electric field at a point. Thus running a Huygens-Fresnel simulation gives the solution to Eq. (1.3).

This is the principle that underpins the algorithm that allows various complex beams, and wave phenomena to be simulated within a ballistic method. The following sections validate the method against the theory and experimental data for various complex beam propagation.

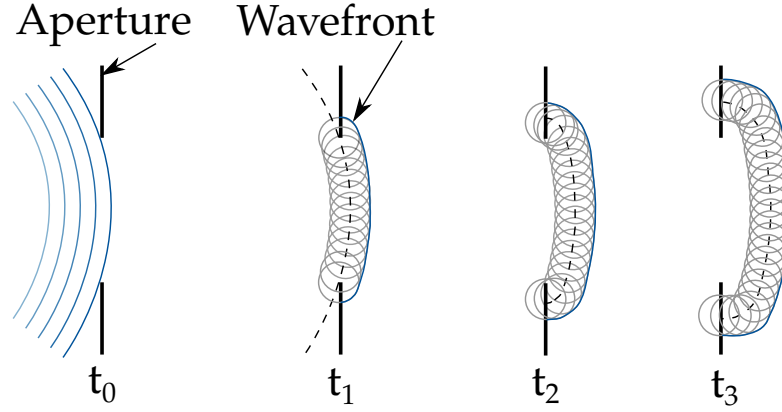


**Figure 1.2:** Illustration of the Huygens-Fresnel principle. At  $t_0$  a wave is incident on an aperture. Times  $t_1$ ,  $t_2$ , and  $t_3$  show the evolution of the wavefront using the Huygens-Fresnel principle.

### 1.2.2 Validation of Phase Tracking Algorithm

#### Double Slit Experiment

The first test of our phase tracking algorithm, is to compare our simulation to a double slit experiment. The double slit experiment, is a simple experiment where monochromatic plane wave of light is incidence on two slits distance apart  $a$ , and width  $b$ , and the interference pattern is observed on a screen a distance  $d$  away from the slits.

This experiment, first carried out by Thomas Young and thus sometimes called Young's slits experiment, is usually carried out with the detector screen in the far field. The so called Fraunhofer regime. The intensity pattern on the detector screen is as in Eq. (1.4):

$$I(\theta) \propto \cos^2 \left( \frac{\pi d \sin \theta}{\lambda} \right) \text{sinc}^2 \left( \frac{\pi b \sin \theta}{\lambda} \right) \quad (1.4)$$

Where the *sinc* function is defined as  $\frac{\sin(x)}{x}$ , for  $x \neq 0$ ,  $d$  is the slit separation and  $\theta$  is the angular spacing of the fringes.

The simulation was carried out for a wavelength of  $\lambda$ , a slit width of  $b$ , and a slit separation of  $d$ . Using the Huygens-Fresnel principle, each slit is a source of Huygens wavelets. The initial position of the photon packets is sampled uniformly from the slit area, after randomly choosing one of the slits. A random direction is then chosen to ensure that the packets will hit the detector screen. The simulation was run with photon packets, which took to run on an 8 core Intel Xeon machine. This gave an accurate match to the theoretical expression, as seen in Fig. 1.3.

**Figure 1.3:** Comparison of theory and simulation for the double slit experiment.  $\lambda$  is  $xnm$ ,  $b$  is  $\mu m$ , and  $d$  is  $mm$ .

#### Diffraction by a Square Slit

$\varphi MC$  is also validated by simulating diffraction from a square aperture in the far and near field, the so call Fresnel and Fraunhofer regimes. Fresnel diffraction occurs in the near field when the

*Fresnel number*, Eq. (1.5), is greater than 1.0. Fraunhofer diffraction occurs when the *Fresnel number* is less than 1.0.

$$F = l\sqrt{\frac{2}{\lambda r_0}} \quad (1.5)$$

Equation (1.5) is the Fresnel number, a measure of whether diffraction is in the Fresnel regime or the Fraunhofer regime.  $l$  is the slit width,  $\lambda$  is the wavelength of the incident radiation, and  $r_0$  is the distance from the aperture to the detector screen, as shown in Fig. 1.4.

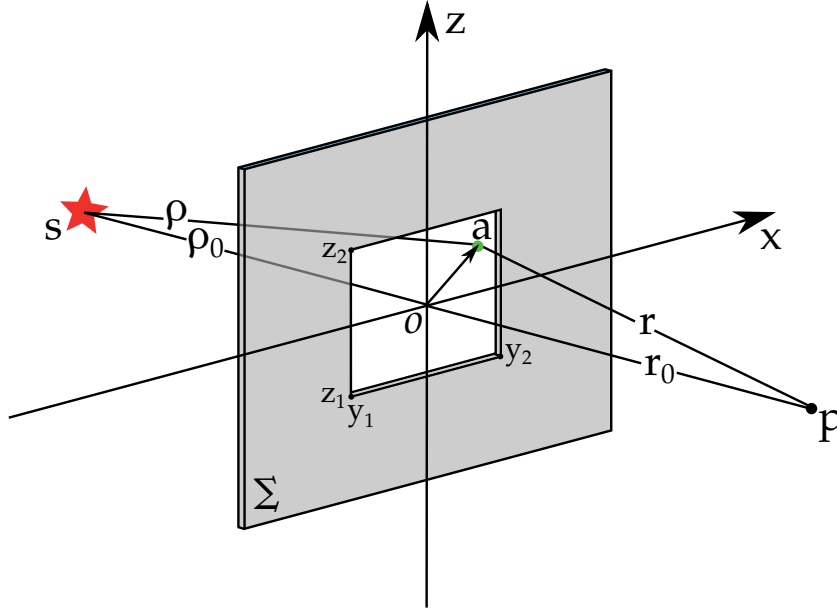


**Figure 1.4:** *Fresnel diffraction at a square aperture.*

In order to compare  $\varphi MC$  to the theory, the theory must first be examined. Consider the setup as shown in Fig. 1.4, in order to calculate the intensity at a point  $P$ , the contribution by an area element  $dS$  at the point  $a$ , to the optical disturbance at a point  $P$  is considered. Accounting for the the unobstructed optical disturbance from  $S$  as well, yields:

$$U(P) = \frac{1}{i\lambda} \iint_{\Sigma} \frac{Ae^{i(k\rho - \omega t)}}{\rho} \frac{e^{ikr}}{r} \cos(\theta) dS \quad (1.6)$$

In the case where  $\rho_0$  and  $r_0$  are large compared to the size of the aperture, then  $\cos(\theta) = 1$  and  $\frac{1}{\rho r} = \frac{1}{\rho_0 r_0}$ . The lengths of  $r_0$  and  $\rho_0$  are:

$$r = \sqrt{r_0^2 + y^2 + z^2} \quad (1.7)$$

$$\rho = \sqrt{\rho_0^2 + y^2 + z^2} \quad (1.8)$$

Using the binomial theorem to expand Eqs. (1.7) and (1.8) yields:

$$\rho + r \approx \rho_0 + r_0 + (y^2 + z^2) \frac{\rho_0 r_0}{2\rho_0 r_0} \quad (1.9)$$

Substituting Eq. (1.9) into Eq. (1.6) with  $k = 2\pi/\lambda$

$$U(P) = \frac{Ae^{-i[k(\rho_0+r_0)\omega t]}}{i\lambda\rho_0 r_0} \iint_{\Sigma} e^{i2\pi y^2 \frac{(\rho_0+r_0)}{2\lambda\rho_0 r_0} + i2\pi z^2 e^{\frac{i\pi u^2}{2}} \frac{(\rho_0+r_0)}{2\lambda\rho_0 r_0}} dS \quad (1.10)$$

Introducing the dimensionless variables  $u$  and  $v$

$$u = y \sqrt{\frac{2(\rho_0 + r_0)}{\lambda\rho_0 r_0}} \quad (1.11)$$

$$v = z \sqrt{\frac{2(\rho_0 + r_0)}{\lambda\rho_0 r_0}} \quad (1.12)$$

and substituting them into Eq. (1.10).

$$U(P) = \frac{\tilde{E}_u}{2} \int_{u_1}^{u_2} e^{\frac{i\pi u^2}{2}} du \int_{v_1}^{v_2} e^{\frac{i\pi v^2}{2}} dv \quad (1.13)$$

Equation (1.13) describes the optical disturbance at the point  $P$ , with  $\tilde{E}_u$  the unobstructed disturbance at  $P$ . Equation (1.13) can be evaluated using the Fresnel integrals,  $C(w)$  and  $S(w)$ :

$$\int_0^w e^{i\pi w'^2/2} dw' = C(w) + iS(w) \quad (1.14)$$

$$S(w) = \int_0^w \sin\left(\frac{\pi w'^2}{2}\right) dw' \quad (1.15)$$

$$C(w) = \int_0^w \cos\left(\frac{\pi w'^2}{2}\right) dw' \quad (1.16)$$

Using Eq. (1.14), where  $C(w)$  and  $S(w)$  are the Fresnel integrals as in Eqs. (1.15) and (1.16), Eq. (1.13) can then be transformed into an intensity, by taking the absolute value and squaring, yielding Eq. (1.17):

$$I_p = \frac{I_u}{4} \{[C(u_2) - C(u_1)]^2 + [S(u_2) - S(u_1)]^2\} \times \{[C(v_2) - C(v_1)]^2 + [S(v_2) - S(v_1)]^2\} \quad (1.17)$$

Equation (1.17) gives the intensity of the field at the point  $P$  on axis for a square aperture where  $I_u$  is the unobstructed intensity at the point  $P$ .

As the mathematics of calculating the optical disturbances at all points on a plane at point  $P$  is difficult, instead the aperture is moved by small displacements, with  $\overrightarrow{SOP}$  fixed. This effectively achieves the translation of the origin,  $O$ , with respect to the fixed aperture. Thus, for each displacement new aperture coordinates  $y_1, y_2, z_1$ , and  $z_2$  are generated and therefore new  $u_1, u_2, v_1$ , and  $v_2$ . Therefore the intensity at a point  $P + \delta d$ , where  $\delta d$  is the displacement, can be calculated. This approximation holds for displacements that are small compared to the  $\rho_0$  [8, 12, 13]. Using this method and Eq. (1.17) gives the theoretical curves in Fig. 1.5.



In  $\varphi MC$ , the above experiment is simulated. A square slit is uniformly sampled in the  $y$ , and  $z$  direction in order to get the packets initial position. A random direction is then sampled, ensuring that the direction points towards the detector screen.

The detector screen's distance from the aperture is then varied and the intensity on the screen is measured for  $\sim 10^{10}$  photons released from the aperture, as Huygens wavelets. For *Fresnel numbers* greater than 1.0, the number of bins is 300, covering a distance of  $600 \mu m$ . For the case of Fraunhofer diffraction, the number of bins is 100 covering a distance of  $6000 \mu m$ . The simulations take  $\sim 3$  minutes for  $10^{10}$  packets to be run on an Intel Xeon E3-1245 v5, 8 cores @ 3.5GHz machine. The number of bins, and photons packets simulated had to be increased for the cases where the Fresnel number was large (i.e the detector screen was near the aperture) Fig. 1.5 shows the comparison between the theory and the  $\varphi MC$  simulations.

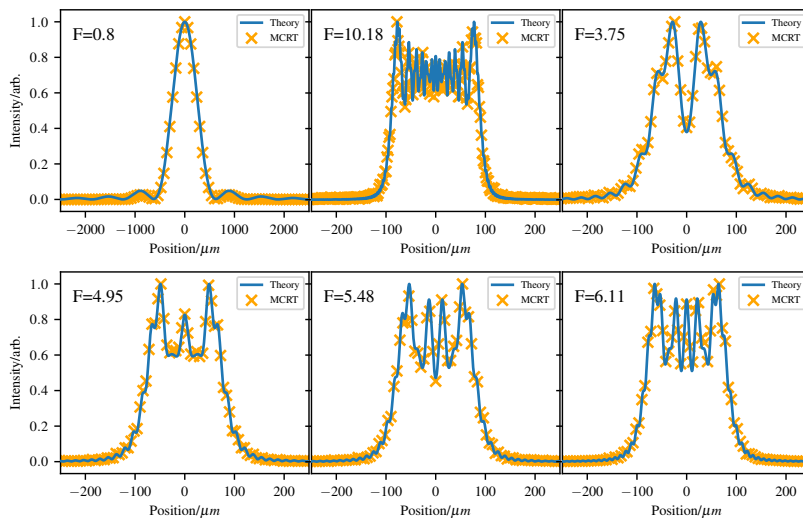


**Figure 1.5:** Comparison of theory and simulation for diffraction through a square aperture in the Fresnel and Fraunhofer regimes.

### 1.3 Gaussian Beams

Now that the method of tracking the phase of photon packets has been verified against theoretical results, we can now turn our attention to modelling the propagation of beams that require the wave behaviour of light in order to either form or propagate.

The first beam type we will examine is the Gaussian beam. Traditional MCRT cannot model Gaussian beams, as Gaussian beams have a finite beam waist at their focus (see Fig. 1.6). MCRT (along with geometric optics) predicts that Gaussian beams have an infinitely small waist. Various authors have tried to model Gaussian beams in a MCRT or geometric optics regime. Some of the techniques used by these authors include: artificial beam steering [14], generating skew rays [15] ...\*\*blab However all these techniques fail in one way or another to accurately model all the physical phenomena presented by a Gaussian beams. This section will show that  $\varphi MC$  can accurately model all the physical phenomena of Gaussian beams, within the MCRT regime.

Before modelling a Gaussian beam, the theory and various physical parameters must be described. The electric field of a Gaussian beam can be defined as in Eq. (1.18):

$$E(r, z) = E_0 \frac{w_0}{w(z)} e^{\frac{-r^2}{w(z)^2}} e^{-i(kz + k \frac{r^2}{2R(z)} - \varphi(z))} \quad (1.18)$$

Where:

$r$  is the radial distance from the optical axis [m];

$z$  is the axial distance from the beams waist [m];

$k$  is the wavenumber,  $k = \frac{2\pi}{\lambda}$  [ $m^{-1}$ ];

$E_0$  is the electric field amplitude at the origin [ $Vm^{-1}$ ];

$w(z)$  is the radius of the beam at which the amplitude has fallen to  $\frac{1}{e}$ , at the distance  $z$  along the beam, Eq. (1.19) [m];

$w_0$  is the waist radius [m];

$R(z)$  is the radius of curvature of the beams wavefronts at  $z$ , Eq. (1.20) [m];

and finally,  $\varphi(z)$  is the Gouy phase at  $z$ , Eq. (1.21) [-].

Equations (1.19) to (1.23) give the definitions of key physical properties as outlined above or as shown in Fig. 1.6.  $z_r$  is the Rayleigh length, Eq. (1.22), and defines the point in which the beams waist grows to  $\sqrt{2}$  times the size of the beam at its waist. The waist of the beam at the focal point is defined as Eq. (1.23), where  $f$  is the focal length and  $D$  is the  $\frac{1}{e^2}$  diameter of the beam at the lens.

$$w(z) = w_0 \sqrt{1 + \left(\frac{z}{z_r}\right)^2} \quad (1.19)$$

$$R(z) = z \left[ 1 + \left(\frac{z_r}{z}\right)^2 \right] \quad (1.20)$$

$$\varphi(z) = \arctan\left(\frac{z}{z_r}\right) \quad (1.21)$$

$$z_r = \frac{\pi w_0^2}{\lambda} \quad (1.22)$$

$$w_0 = \frac{2\lambda f}{\pi D} \quad (1.23)$$

$$(1.24)$$

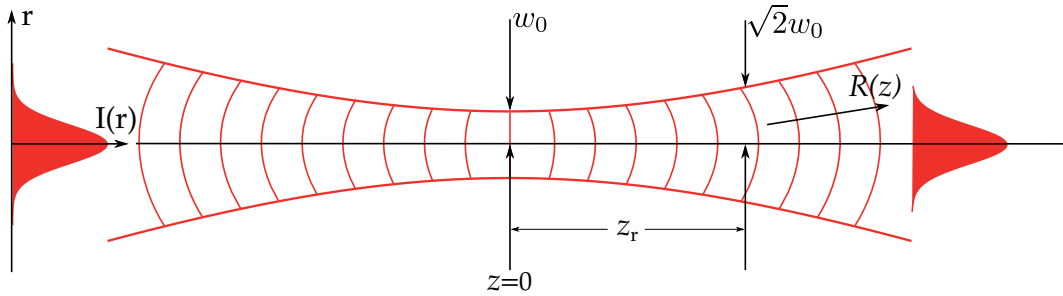


**Figure 1.6:** Illustration of a Gaussian beam focusing to its waist then diverging away. Image shows the various defined properties of a Gaussian beam along side the radius of curvature changing direction at the waist.

With the physical properties of the Gaussian beam outlined, a Gaussian beam can now be modelled using our algorithm. In order to simulate the Gaussian beam, we set up the simulation as shown in Fig. 1.7. The lens used is convex-plano lens, with radius of curvature,  $4.6 \text{ mm}$ , thickness,  $L_t$ , of  $2.2 \text{ mm}$ , and working distance,  $W_d$ ,  $8.5 \text{ mm}$ . A Gaussian beam wavelength  $488 \text{ nm}$  and  $\frac{1}{e^2}$  waist diameter  $0.5 \text{ mm}$ , is incident on the lens. Using Eq. (1.23) yields the size of the focal spot as  $3 \mu\text{m}$ .

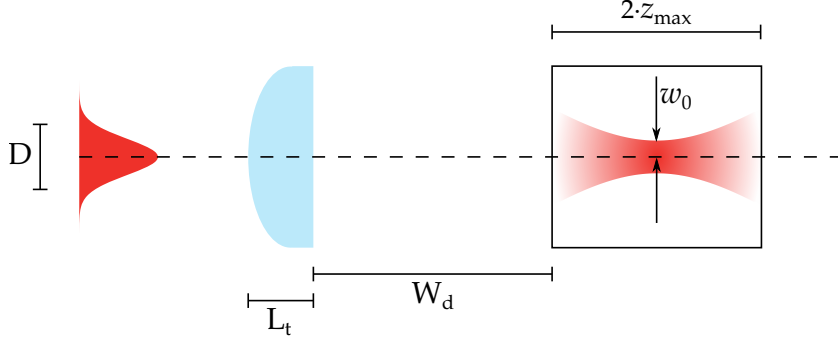


**Figure 1.7:** Simulation setup of focusing a Gaussian beam through a lens. Lens is convex-plano and is modelled on ThorLabs LA4249 UV fused silica lens [16].

To model the lens in  $\varphi$  the photons initial  $z$  position is set just in front of the lens. The  $x$  and  $y$  are randomly sampled from a Gaussian distribution with a waist of  $\sqrt{2}w_0$ . The factor of  $\sqrt{2}$  accounts for the conversion from intensity to electric field beam waist. This is due to the fact that the electric field is  $\propto e^{\frac{-r^2}{4\sigma'^2}}$ , and the intensity is  $\propto e^{\frac{-r^2}{2\sigma'^2}}$ . Thus for the input electric field waist to be equal to the intensity waist, i.e  $\sigma' = \sigma$ ,  $\sigma' = \sqrt{2}\sigma$ .

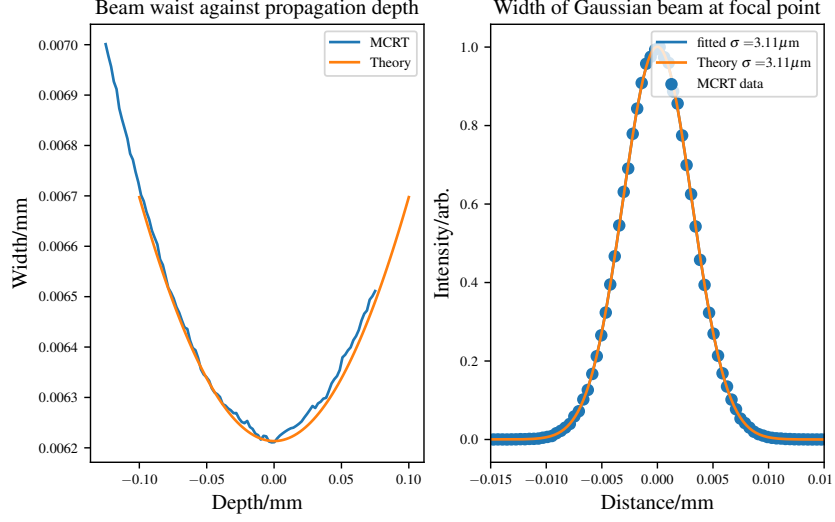
The photon is then propagated to the surface of the convex side of the lens. This is achieved by finding the intersection of a sphere which represents the convex side of the lens, and the packets path. With the packet on the surface of the lens, Fresnel coefficients are calculated to determine if the packet is reflected or refracted. If the packet is reflected the packet is killed and the process starts again. If the packet is refracted, and moved in the new direction to the planar surface of the lens. The new direction vector is calculated using a vector version of Snell's law, as shown in ???. The packets is then uniformly sampled onto the surface of the voxel medium and the usual MCRT method is used to propagate the packet whilst tracking the phase.

Figure 1.8 shows the comparison of theory and *in-silico* experiment, with excellent agreement between the two.

$\varphi MC$  also correctly models the change of direction of the radius of curvature,  $R(z)$ , as is predicted by theory. This can be seen in Fig. 1.9

$\varphi MC$  can also model spherical aberrations caused by lenses. Fig. 1.10 shows aberrations caused by a plano-convex lens.

This section has shown that Gaussian beams, and their physical phenomena can be accurately modelled using  $\varphi MC$ . A convex-plano lens was used to focus a Gaussian beam, but it is simple to implement other other lenses given a triangulated mesh of the lens or an equation that describes the shape of the lens.



**Figure 1.8:** Results of in-silico experiment of focusing a Gaussian beam through a convex-plano lens.  $L_t$  is the lens thickness,  $D$  is the  $\frac{1}{e^2}$  input beam diameter,  $W_d$  is the working distance or back focal length,  $2z_{max}$  is the depth of the medium, and  $w_0$  is the beam waist.

**Figure 1.9:** Slice through the real part of the complex electric field of the in-silico experiment as in Fig. 1.7. Figure shows the radius of curvature changing direction at the waist as predicted by theory.

**Figure 1.10:** Illustration of  $\varphi MC$ 's ability to model spherical aberrations. Image generated using same setup as in Fig. 1.7, but with a  $D = 2$  mm.

## 1.4 Bessel Beams

Bessel beams, as described in the introduction to this chapter, are “non-diffracting” beams, that can “self heal”. This means, in reality, that the central core of the beam does not spread out, and that if a blockage is placed in front of the beam, the beam reforms further down the optical axis. There is some debate amongst physicists as to whether these phenomena are justly labelled, or if they are terms used to make Bessel beams seem like the solution to everything.

The first “complex” beam simulated using  $\varphi MC$  is a Bessel beam. Bessel beams are non-diffractive solutions to the wave equation. Bessel beams were first shown to

From the scalar description of the electric component of the beam, we get:

$$E(r, z) = E_0 \sqrt{\frac{2\pi k z w_0 \sin(\beta)}{z_{max}}} \exp\left(-\frac{z^2}{z_{max}^2} - \frac{i\pi}{4}\right) J_0(kr \sin(\beta)) \exp(ikz \cos(\beta)) \quad (1.25)$$

Where:

$k$  is the wavevector,  $k = \frac{2\pi}{\lambda}$  [m];

$z$  is the distance from the axicon tip [m];

$\beta$  is the angle the wavefront propagates at (see Fig. 1.11) [rad];

$w_0$  is the  $\frac{1}{e^2}$  width of the input Gaussian beam [m];  
 $J_0$  is the Bessel function of the first order;  
 $r$  is radial distance from the optical axis [m].

Equation (1.25) gives the electric field for a Bessel beam. The intensity can be calculated using:

$$I(r, z) = \frac{c\epsilon_0 |E|^2}{2} \quad (1.26)$$

Using the definition total power transmitted by a beam as:

$$P = \frac{\pi I_0 w_0^2}{2} \quad (1.27)$$

Where  $I_0$  is defined as on axis intensity of the incident Gaussian beam.

$$I_0 = \frac{c\epsilon_0 E_0^2}{2} \quad (1.28)$$

Substituting Eqs. (1.25), (1.27) and (1.28) into Eq. (1.26) yields:

$$I(r, z) = \frac{4k_r P}{w_0} \frac{z}{z_{max}} J_0^2(k_r r) \exp\left(-\frac{2z^2}{z_{max}^2}\right) \quad (1.29)$$

Where:

$k_r$  is the radial wavevector,  $k_r = k \sin(\beta)$ ;  
 $P$  is the power of the incident Gaussian beam.

Bessel beam can be formed by an axicon lens or by diffraction through a ring. All the simulations of Bessel beams in this thesis use the axicon method of generating a Bessel beam, thus only axicons will be discussed. Figure 1.11 shows the geometry of a Bessel beam formed by an axicon. Using simple geometry and Snell's law the following equation can be derived to describe various properties of a Bessel beam formed by an axicon [?, 17].

The propagation depth of a Bessel beam is defined as the distance from the tip of the axicon to the end of the "Bessel region". However in reality the Bessel beam will continue to propagate slightly passed this depth. Equation (1.30) shows the propagation depth of a Bessel beam where  $\cot$  is the cotangent function.

$$z_{max} = R(\cot(\beta) - \tan(\alpha)) \quad (1.30)$$

The propagation angle of the conical waves,  $\beta$  can be calculated using Snell's law and  $\alpha$  the angle of the axicon:

$$\beta = \arcsin(n \sin(\alpha)) - \alpha \quad (1.31)$$

The central core of a Bessel beam is defined as the distance to the first zero of the Bessel beam. Equation (1.32) shows the radius of the core, where 2.405 is derived from position of the first zero of the Bessel function.

$$r_o = \frac{2.405}{k \sin(\beta)} \quad (1.32)$$

Finally, the spacing between Bessel beam rings is:

$$\Delta\rho = \frac{\lambda}{2 \sin(\beta)} \quad (1.33)$$

### 1.4.1 Validation

To ensure that the method described in Section works as intended for Bessel beams several tests are run against theoretical expressions and experimental data.

#### Comparison to theoretical Bessel beam

To compare against a theoretical Bessel beam, a Bessel beam is modelled in the MCRT phase simulation, and propagated through air into the “Bessel region” and then propagated into the far field to ensure the beam follows the theory in both these regions.

Figure 1.11 shows the setup for the *in-silico* experiments. The Bessel beam is created with an axicon (conical) lens with an opening angle ( $\alpha$ ) of  $5^\circ$ , and a radius of  $12.7\text{ mm}$ . The input beam is Gaussian in profile with a  $\frac{1}{e^2}$  diameter of  $1\text{ mm}$ , and a wavelength of  $488\text{ nm}$ . The Bessel beam is then propagated to a detector screen  $10\text{ mm}$  away from the tip of the axicon, which is in the middle of the “Bessel region” for the first test. for the second test the Bessel beam is propagated past the “Bessel region” into the far field. The detector screen has a size of  $40\text{ mm} \times 40\text{ mm}$  with a bin resolution of  $1\text{ }\mu\text{m}$ .  $8^{10}$  photon packets were simulated taking  $\sim 1$  hour on an 8 core Intel Xeon 3.5Ghz machine.

Equation (1.29) gives the profile of a theoretical Bessel beam at a depth  $z_{max}$ , this is plotted against the simulation when  $\frac{4k_r Pz}{w_0 z_{max}} e^{-2\left(\frac{z}{z_{max}}\right)^2} = 1$ , with the simulation similarly normalised, by normalising to the maximum intensity of the image generated. Figure 1.12 shows this comparison.

Figure 1.13 shows the profile of the Bessel beam in the far field, where the theory predicts that it becomes a circular beam.

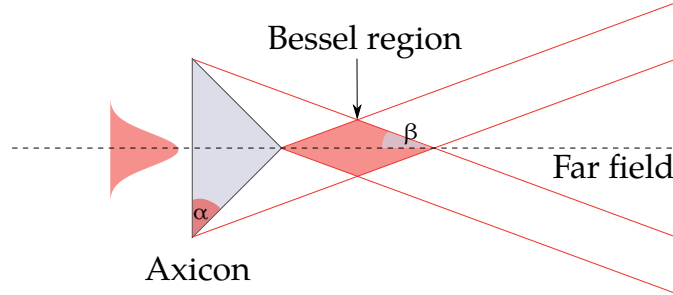


**Figure 1.11:** Geometry of a Bessel beam, generated by an axicon lens.  $\beta$  is the angle with the optical axis, and the angle of the conical waves.  $\alpha$  is the axicon angle.

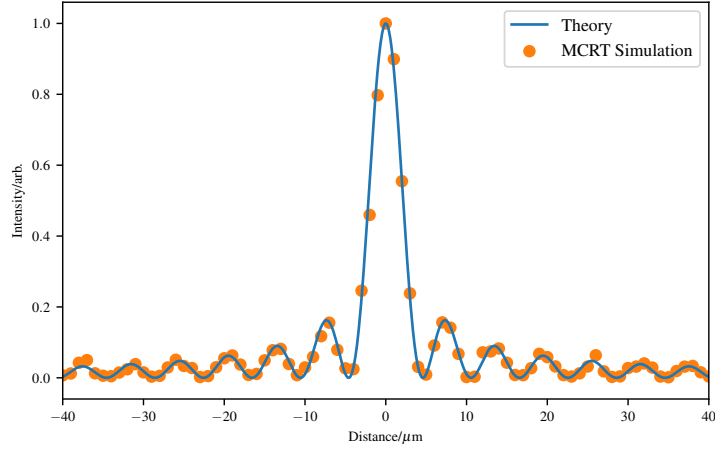


**Figure 1.12:** Comparison of theoretical and MCRT simulation of a Bessel beams, with intensity normalised. The results from  $\varphi$ MC show good agreement with the theory.

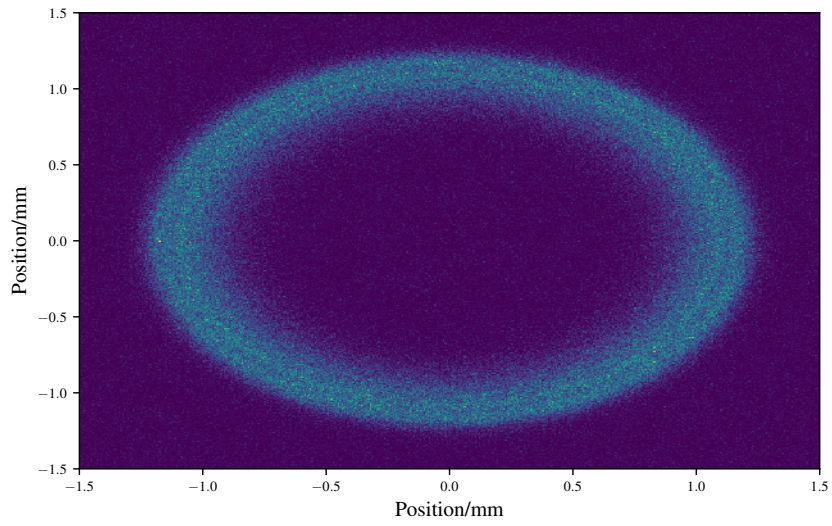


**Figure 1.13:** Bessel beam in the far field.

### Comparison to experimental data

To ensure our algorithm works in turbid media, we carried out an experiment where a Bessel beam was propagated through a medium of varying turbidity. A laser, wavelength  $488\text{ nm}$ , with a Gaussian profile is shone on an axicon lens, with angle  $5^\circ$ . The laser beam had a  $\frac{1}{e^2}$  diameter of  $2\text{ mm}$ . The Bessel beam was allowed to propagate through the air for  $10\text{ cm}$  before entering a cuvette of side  $2\text{ mm}$ . The cuvette was filled with  $500\text{ }\mu\text{L}$  of water, and various volumes of a scattering agent added. The scattering agent used is intralipid 20 % (Sigma-Aldrich), which is diluted as shown in Table 1.1. Figure 1.15 shows the optical properties of Intralipid 20 %. Dilutions of Intralipid are kept below 2% scattering particle concentration, so that the scattering exhibited by the intralipid is in the independent scattering regime. This allows the linear scaling of the optical properties by concentrations [18–20]. Images of the Bessel beam as it emerges from the cuvette are taken for comparison with our algorithm. Figure 1.14 shows the experimental setup.

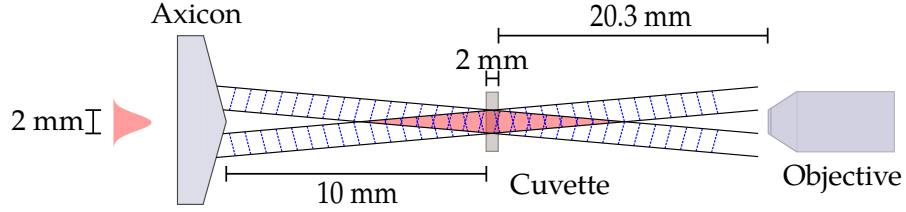


**Figure 1.14:** Experimental setup for propagating a Bessel beam through a cuvette filled with varying concentrations of Intralipid 20%. Bessel beam is imaged by an  $20\times$  objective lens and a Grasshopper 3 camera.

Volume/ $\mu\text{L}$ Intralipid	$\text{H}_2\text{O}$	Intralipid concentration		Optical properties
		Volume/%	Scattering particle/%	Scattering coefficient/ $\text{m}^{-1}$
0	500	0.00	0.00	0.00
2	500	0.39841	0.0908	557.14
4	500	0.79365	0.1816	1114.28
6	500	1.18577	0.2724	1671.42
8	500	1.57480	0.3632	2228.56
10	500	1.96078	0.4534	2785.71
12	500	2.34375	0.5448	3342.84

**Table 1.1:** Intralipid solutions used for experiment.

To model within  $\varphi\text{MC}$ , the experimental setup we simplify the setup considerably. The simulation models the propagation of a photon packet through the axicon to its conical surface. On the conical surface the Huygens-Fresnel principle is invoked, and the packet is sampled onto the surface of the medium (cuvette). The sampling of the photon onto the surface of the medium, speeds the algorithm up, as it does not need to simulate the photons that would “miss” the medium. From there the usual MCRT method propagates the packet through the medium while tracking its phase, and scattering the packet until it leaves the medium. If the packet leaves the medium to any side other than the far side of the cuvette (e.g any side of the cuvette not facing the objective lens), then it is discarded. If the packet leaves the medium on the objective lens facing side, then the packet is recorded by its phase onto an area element. For each intralipid concentration  $6.4 \times 10^{10}$  photons are run over 64 cores, taking  $\sim 3$  hours for



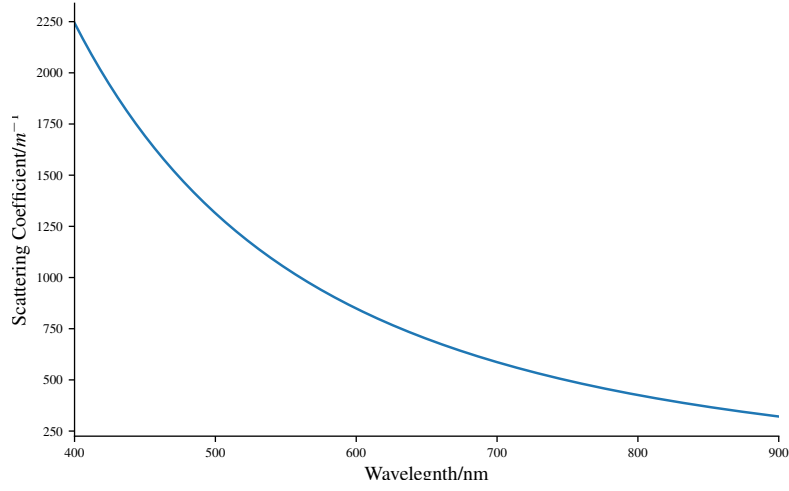


**Figure 1.15:** Scattering properties of 20% Intralipid [21].

the 0.5448% intralipid concentration. Once all the photon packets have been run, the phase is converted into intensity, as in Eq. (1.2), but in 2D.

Figure 1.16 shows the results from the experiment and simulation. The simulation shows good agreement with experimental data.

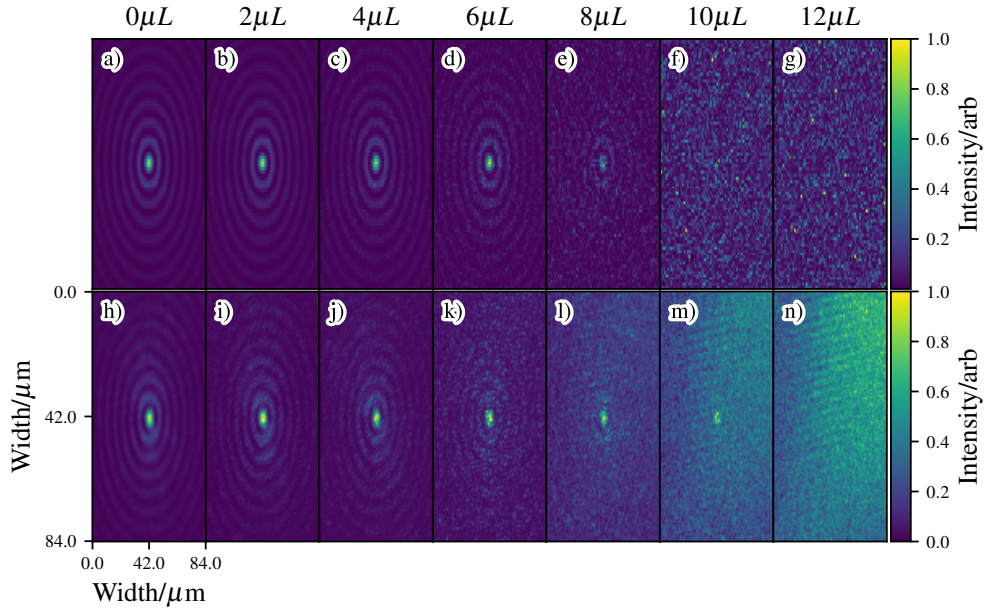


**Figure 1.16:** Comparison of experimental and simulation data for propagation of a Bessel beam produced by an axicon, through mediums of various turbidity. Images a) to g) is the data from  $\varphi MC$ , and h) to n) are the experimental data. Volumes along the top is the volume of Intralipid in each solution as in Table 1.1. All images cropped so they are the same size.

## Discussion

Originally the medium was modelled as in the experiment, a  $2\text{ mm}^3$  volume. The image created was thus a  $2001 \times 2001$  with a resolution of  $1\text{ }\mu\text{m}$ . In order to achieve a good signal to noise ratio for this setup  $6.4 \times 10^{12}$  packets needed to be run, taking  $\sim 70$  hours on a computer cluster using 64 cores. This was enough packets to get a good signal to noise ratio on all the simulations up to  $6\text{ }\mu\text{L}$ . However the amount of packets needed to get a good signal to noise ratio for  $8\text{ }\mu\text{L}$  and above was prohibitively computationally costly. Therefore the modelled medium was shrunk in the  $x$  and  $y$  directions giving:  $0.5\text{ mm} \times 0.5\text{ mm} \times 2.0\text{ mm}$ . This allowed a smaller image ( $501 \times 501$ ), whilst keeping the same resolution. Shrinking the medium also has the benefit that the photons are confined closer to the image plane, thus ensuring more photons are hit the plane in comparison to the larger medium.

Shrinking the mediums size does have some draw backs. Firstly Bessel beams propagation depth rely on the input beams width see Eq. (1.30). The input beams width was kept constant between the shrinking of the volumes size. However shrink the mediums size in the  $x$  and  $y$  directions gives the same effect as using a smaller input beam. Therefore the  $x$  and  $y$  dimension were carefully chosen such that the Bessel beam would still form a Bessel beam at the image plane. The second issue with shrinking the medium is that some packets may be lost. What this means is that, in the larger medium a packet may scatter towards an  $x$  or  $y$  medium wall and then scatter back into the centre of the medium and then is recorded. However this same packet in the smaller medium would be lost as the packet would exit the medium and ceased to be tracked. It is not expected that this will cause much of an issue as any scattering event already degraded the quality of the beam, as that packet is no longer coherent with the rest of the packets, thus it will not contribute positively to the Bessel beam. To ensure this is not an issue, results from a larger medium are compared to that of the smaller medium in Fig. 1.17. The larger and smaller medium yield the same results (within Monte Carlo noise) for Intralipid volumes less than  $8\text{ }\mu\text{L}$ . At  $8\text{ }\mu\text{L}$  the smaller medium has a Bessel beams central core, whilst the larger medium is noisy, and forms no Bessel beam. This test has shown that shrinking the medium allows accurate modelling of the propagation of a Bessel beam through a turbid medium while using less computational resources.

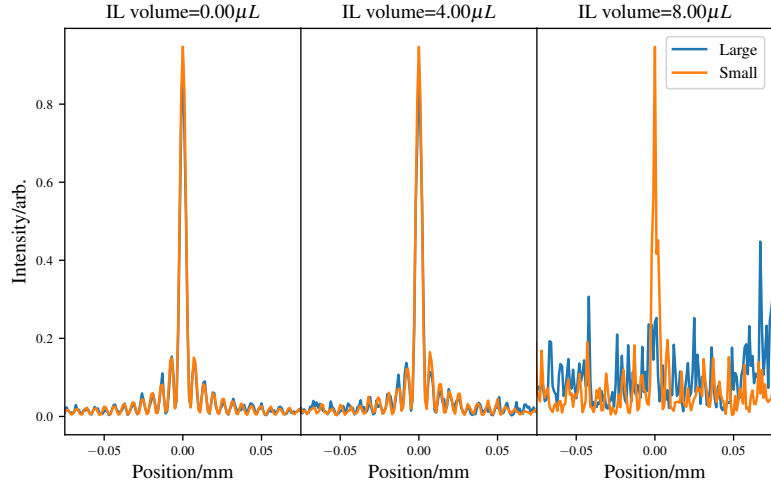


**Figure 1.17:** Comparison of a larger medium,  $2\text{ mm}^3$  versus that of a smaller medium,  $0.5\text{ mm} \times 0.5\text{ mm} \times 2.0\text{ mm}$ .

## 1.5 Higher order Bessel beams

Our technique outlined in the preceding sections, can also be applied to arbitrary higher order Bessel beams.

The electric field of a Bessel beam is:

$$E(r, \varphi, z) = E_0 J_l(k_r r) e^{-ik_z z} e^{-il\varphi} \quad (1.34)$$

Where:

- $l$  is the order of the beam [-];
- $k_z^2 + k_r^2 = k^2$ , where  $k^2$  is the wavevector [ $m^{-1}$ ];
- $r, \varphi, \text{ and } z$  are the cylindrical coordinates [ $m, \text{rad}, m$ ];
- and  $J_l$  is the  $l$ -order Bessel function of the first kind [-].

To generate higher order Bessel beam, a helicon is used. A helicon (shown in Fig. 1.18) is an axicon attached to a helix phase delay element. The helical element imparts a helical phase delay to photon packets as they pass through the element.

The distance travelled though the helicon is shown in Eqs. (1.35), (1.36) and (1.38) [22].  $h_1$  is the path length travelled by a photon through the helical element.  $h_2$  is the path through an axicon.

$$h_1 = \frac{l\varphi\lambda}{(n-1)2\pi} \quad (1.35)$$

$$h_2 = r \tan(\alpha) \quad (1.36)$$

$$h_3 = h_1 + h_2 \quad (1.37)$$

$$\Delta h = \frac{l\lambda}{n-1} \quad (1.38)$$

Where  $\varphi$  is the azimuthal angle,  $r$  is the radial position,  $l$  is blah, and  $\alpha$  is the axicon angle.

The path length in the above equations can be converted into a phase delay by considering the transmission functions of the individual elements [23–26]:

$$T_1(\varphi) = e^{-ik(n-1)h_1} = e^{-il\varphi} \quad (1.39)$$

$$T_2(r) = e^{-ik(n-1)h_2} = e^{-ik_r r} \quad (1.40)$$

$$T_3(r, \varphi) = T_1 * T_2 = e^{-ik_r r - il\varphi} \quad (1.41)$$

$$(1.42)$$

Where  $T_1$  is the transmission function for the helical element,  $T_2$  is the transmission function for the axicon, and  $T_3$  is the total transmission function. Using the small angle approximation for  $\beta$  and Eq. (1.31), and knowing  $k_r = \sin(\beta)$  yields the phase delay as a function of angle and radial position:

$$\phi(\varphi, r) = k(n-1)r\alpha + l\varphi \quad (1.43)$$

To implement a helicon in the  $\varphi MC$  algorithm, an additional helical phase delay is added. The additional delay is implemented by adding  $l\varphi$  where  $0 < \varphi < \frac{2\pi}{l}$ . An actual helix element is not modelled explicitly in the code, but rather just the phase delay. This method is similar to using a spatial light modulator in an experiment to impart a phase delay on a beam.

Figure 1.19 shows the comparison between theoretical higher order Bessel beam and the higher order beam beam simulated by  $\varphi MC$ .

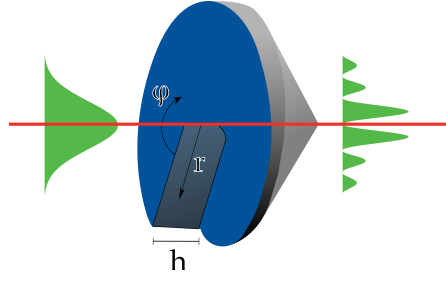


**Figure 1.18:** Helical delay element attached to an axicon. Axicon introduces an additional radial delay in addition to that of the helical element. Input beam is a Gaussian, output beam is a higher order Bessel beam,  $l > 0$ .

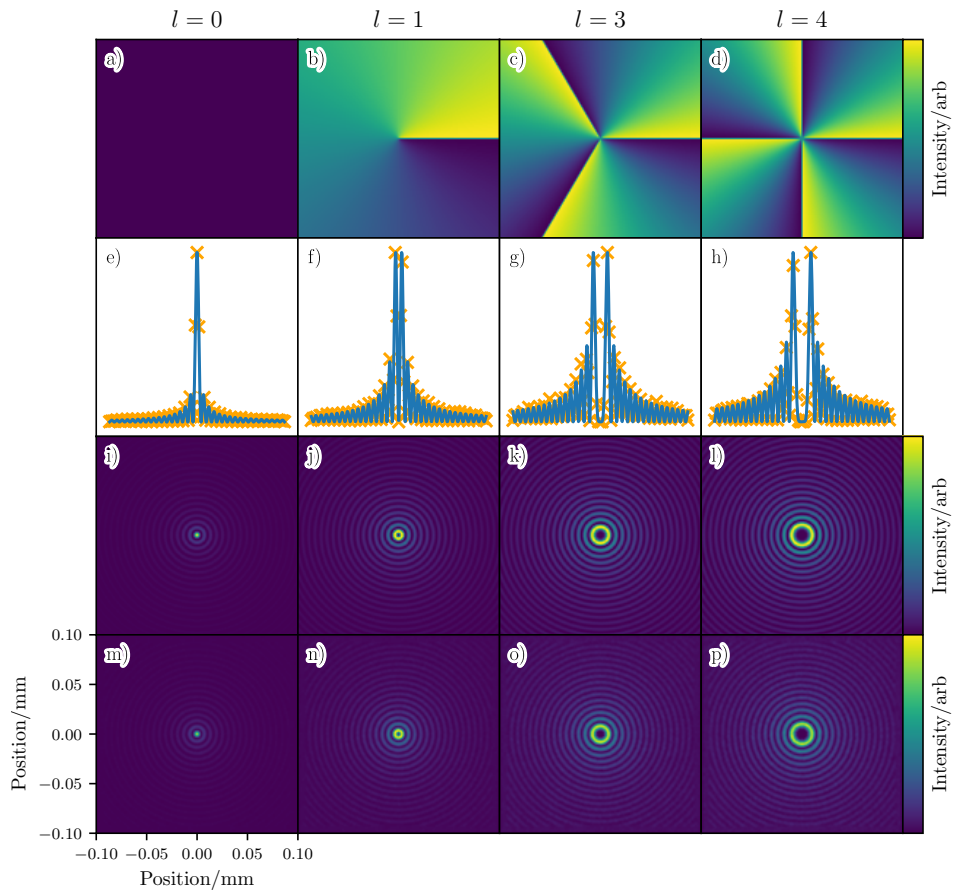


**Figure 1.19:** Higher order Bessel beams. a) to d) show the phase shift due to the helical element. e) to h) show line plots of the simulation data compared to the theory. i) to l) and m) to p) show the higher order Bessel beam images for theory and simulation data respectively.

## **1.6 Comparison**

## **1.7 Discussion**

a [\[27\]](#)

## **1.8 Conclusion**



# Bibliography

- [1] Jörg Baumgartl, Michael Mazilu, and Kishan Dholakia. Optically mediated particle clearing using airy wavepackets. *Nature photonics*, 2(11):675, 2008.
- [2] David B Ruffner and David G Grier. Optical conveyors: a class of active tractor beams. *Physical review letters*, 109(16):163903, 2012.
- [3] Tom Vettenburg, Heather IC Dalgarno, Jonathan Nylk, Clara Coll-Lladó, David EK Ferrier, Tomáš Čížmár, Frank J Gunn-Moore, and Kishan Dholakia. Light-sheet microscopy using an airy beam. *Nature methods*, 11(5):541, 2014.
- [4] NB Simpson, L Allen, and MJ Padgett. Optical tweezers and optical spanners with laguerre-gaussian modes. *journal of modern optics*, 43(12):2485–2491, 1996.
- [5] J.M. Durnin, J.J. Miceli Jr, and J.H. Eberly. Diffraction-free beams. *Physical review letters*, 58(15):1499, 1987.
- [6] J.M. Durnin. Exact solutions for nondiffracting beams. I. the scalar theory. *JOSA A*, 4(4):651–654, 1987.
- [7] C. Huygens. *Treatise on light*. tredition, 2012.
- [8] E. Hecht. *Optics*. Pearson Education, Incorporated, 2017.
- [9] C. Huygens, T. Young, A.J. Fresnel, and F. Arago. *The wave theory of light: memoirs of Huygens, Young and Fresnel*, volume 15. American Book Company, 1900.
- [10] A. Fresnel. Mémoire sur la diffraction de la lumière. *da p. 339 a p. 475: 1 tav. ft; AQ 210*, page 339, 1819.
- [11] G. Kirchhoff. Ann. d. physik. (2), 18:663, 1883.
- [12] M. Born, E. Wolf, and A.B. Bhatia. *Principles of Optics: Electromagnetic Theory of Propagation, Interference and Diffraction of Light*. Cambridge University Press, 2000.
- [13] J.W. Goodman. *Introduction to Fourier Optics*. W. H. Freeman, 2017.
- [14] Brett H Hokr, Joel N Bixler, Gabriel Elpers, Byron Zollars, Robert J Thomas, Vladislav V Yakovlev, and Marlan O Scully. Modeling focusing gaussian beams in a turbid medium with monte carlo simulations. *Optics express*, 23(7):8699–8705, 2015.
- [15] Jacques Arnaud. Representation of gaussian beams by complex rays. *Applied optics*, 24(4):538–543, 1985.

- [16] Thorlabs Inc. UV fused silica plano-convex lenses. <https://www.thorlabs.com/thorproduct.cfm?partnumber=LA4249>, 2019. [Online; accessed 18-April-2019].
- [17] F. Merola, S. Coppola, V. Vespini, S. Grilli, and P. Ferraro. Characterization of bessel beams generated by polymeric microaxicons. *Measurement Science and Technology*, 23(6):065204, 2012.
- [18] B. Aernouts, E. Zamora-Rojas, R. Van Beers, R. Watté, L. Wang, M. Tsuta, J. Lammertyn, and W. Saeys. Supercontinuum laser based optical characterization of intralipid® phantoms in the 500-2250 nm range. *Optics express*, 21(26):32450–32467, 2013.
- [19] M.Z. Vardaki, B. Gardner, N. Stone, and P. Matousek. Studying the distribution of deep raman spectroscopy signals using liquid tissue phantoms with varying optical properties. *Analyst*, 140(15):5112–5119, 2015.
- [20] P. Di Ninni, F. Martelli, and G. Zaccanti. Effect of dependent scattering on the optical properties of intralipid tissue phantoms. *Biomedical optics express*, 2(8):2265–2278, 2011.
- [21] R. Michels, F. Foschum, and A. Kienle. Optical properties of fat emulsions. *Optics Express*, 16(8):5907–5925, 2008.
- [22] X. Wei, C. Liu, L. Niu, Z. Zhang, K. Wang, Z. Yang, and J. Liu. Generation of arbitrary order bessel beams via 3d printed axicons at the terahertz frequency range. *Applied optics*, 54(36):10641–10649, 2015.
- [23] S.N. Khonina, V.V. Kotlyar, V.A. Soifer, M.V. Shinkaryev, and G.V. Uspleniev. Trochoson. *Optics Communications*, 91(3-4):158–162, 1992.
- [24] V.V. Kotlyar, A.A. Kovalev, S.N. Khonina, R.V. Skidanov, V.A. Soifer, H. Elfstrom, N. Tossavainen, and J. Turunen. Diffraction of conic and gaussian beams by a spiral phase plate. *Applied optics*, 45(12):2656–2665, 2006.
- [25] S. Topuzoski and L. Janicijevic. Conversion of high-order laguerre–gaussian beams into bessel beams of increased, reduced or zeroth order by use of a helical axicon. *Optics Communications*, 282(17):3426–3432, 2009.
- [26] S. Qiong-Ge, Z. Ke-Ya, F. Guang-Yu, L. Zheng-Jun, and L. Shu-Tian. Generalization and propagation of spiraling bessel beams with a helical axicon. *Chinese Physics B*, 21(1):014208, 2012.
- [27] C. Mignon, A.H. Rodriguez, J.A Palero, B. Varghese, and M. Jurna. Fractional laser photothermolysis using bessel beams. *Biomedical optics express*, 7(12):4974–4981, 2016.